Pore-network study of methane hydrate dissociation

Ioannis N. Tsimpanogiannis* and Peter C. Lichtner
Hydrology, Geochemistry and Geology Group (EES-6), Los Alamos National Laboratory, MS T003, Los Alamos, New Mexico 87545, USA

(Received 22 December 2005; revised manuscript received 29 September 2006; published 8 November 2006)

A two-dimensional pore-network model based on invasion percolation is used to study the patterns obtained from the release of methane during the dissociation of methane hydrates (without including dissociation kinetics) caused by a sudden pressure reduction in the system below the hydrate equilibrium pressure. The concept of the critical gas saturation S_{gc} (volume fraction of the gas phase at the onset of bulk gas flow) is introduced to analyze gas hydrate dissociation. The effects of throat-size distribution (corresponding to off-shore oceanic sediments or on-shore sediments under permafrost), applied pressure difference across the network, and initial hydrate saturation on the resulting gas patterns and on the critical gas saturation are examined to determine the possibility of producing methane. As expected, large throat sizes or wide throat distributions, large pressure drops, and higher initial hydrate saturation act as promoters for the production of the released gas. For typical deep ocean sediments with small pore sizes and low hydrate saturation, it may be difficult to produce methane resulting from hydrate dissociation.

DOI: 10.1103/PhysRevE.74.056303 PACS number(s): 47.55.Kf, 64.60.Ak, 61.43.Hv

I. INTRODUCTION

Clathrate hydrates are crystalline structures that can be formed under conditions of low temperatures or high pressures, both above and below the freezing point of water. They consist of a lattice made up of hydrogen-bonded water molecules containing cavities. The lattice can be stabilized by van der Waals forces through the occupation of specific cavities within the lattice by certain types of guest molecules [1]. Over 100 different guest molecules are known to form clathrate hydrates [2]. This work focuses on methane hydrate and its relation to energy applications.

Interest in clathrate hydrates arises from their capacity to store large volumes of gas. The amount of methane gas that can be stored in hydrate is about 180 times higher compared to the amount of gas at standard conditions [3] in the same volume. This characteristic feature of hydrates has led to considering them for storage and transport of natural gas [4], temporary storage of gas at power plants to be used at peak hours, and hydrogen storage [5]. Furthermore, worldwide accumulations of hydrates containing predominantly methane, including both on-shore (under permafrost) and off-shore (in marine sediments) deposits, provide an enormous reservoir of carbon and represent a large potential source of a cleaner-burning fuel [6], compared to more traditional fuels. Conservative estimates of the amount of methane entrapped in hydrates are on the order of 10^{16} m^3 [7]; however, this value is still being debated in the literature [8]. If these estimates are even approximately correct, a vast amount of carbon is stored in gas hydrates, larger by a factor of 2 than the carbon present in all known fossil fuels combined together [9]. The formation of clathrate hydrates as a by-product of oceanic disposal of carbon dioxide has also been considered as a possible way to remove carbon dioxide from the atmosphere [2,10]. A considerable amount of work has been performed following the pioneering suggestion by Marchetti [11] to investigate the disposal of carbon dioxide by direct injection into the ocean as a means of sequestering this greenhouse gas. Of significant interest (both from an economic and environmental point of view) is the simultaneous disposal of carbon dioxide by injection in ocean sediments, combined with production of methane [12–14]. However, this process has not yet proven to be commercially viable and additional studies are needed. Dissociation of metastable methane hydrates in marine sediments may also affect global climate, since methane, once released, acts as a strong greenhouse gas and can play a significant role in global warming [9,15].

The study of clathrate hydrates has also attracted the attention of the petroleum industry because formation of clathrate hydrates can result in blockage of wells and pipelines in arctic regions, therefore causing a significant economic impact on production [16].

A large number of studies have appeared in the literature as a result of the significant scientific and technological importance of clathrate hydrates. However, due to the complexity of the problem and the interplay of physical and chemical interactions, many issues concerning the interaction of clathrates with the environment remain unresolved. Providing a complete review of the literature is beyond the scope of this work. Excellent reviews on the topic have been provided by Englezos [2], Sloan [18,19], Buffet [6], Koh [17], Makogon [20], and Kvenvolden [9].

Most studies in the clathrate hydrate literature are focused on studying phenomena in the absence of a porous medium. The effect of porous media on the dissociation and/or formation behavior of clathrate hydrates was addressed by only a limited number of studies. Handa and Stupin [21] showed that the dissociation pressures of methane and propane hydrates in 70-Å-radius silica gel pores are higher than in the absence of the porous gel. Additional experiments resulting in similar conclusions were reported by Uchida *et al.* [22,23], Wilder *et al.* [24], Sheshardi *et al.* [25], Smith *et al.* [26], and Anderson *et al.* [27,28]. Tohidi *et al.* [29] con-

*Author to whom correspondence should be addressed. Email address: tsimpano@usc.edu

ducted visualization experiments using two-dimensional transparent glass micromodels and reported that hydrates can form from either free or dissolved gas. They also reported that hydrates usually form within the center of pore spaces (with a thin film of water covering the grains), rather than nucleating on grain surfaces. Theoretical works that considered the effect of sediment on hydrate stability include those by Clarke *et al.* [30] and Klauda and Sandler [31].

The presence of pore-scale phenomena (microscale), however, could introduce additional complexities. In particular, the effect of pore space geometry, pore-network topology and heterogeneity, and pore space accessibility on gas phase mobility needs further investigation. Such issues can influence, among others, the ability to economically produce the released methane gas. To emphasize further the importance of porous sediments, consider that typical pore values found in oceanic sediments are very low [32,33]. For example, Yang and Alpin [33] report for mudstones obtained from the Norwegian margin mean pore throat sizes in the range 8–452 nm and pore throat size standard deviation in the range 9–1425 nm. Note, however, that hydrate occurrence, in addition to fine-grained sediments (as mentioned above), has also been reported in coarser oceanic sediments. A more detailed discussion of this issue is given by Tsimpanogiannis and Lichtner [34]. Larger pore values corresponding to onshore sediments under the permafrost were considered in this study as well.

The presence of a porous sediment may be important in explaining deviations of the observed seismic bottom-simulating-reflector (BSR) depth from hydrate-water-gas equilibrium calculations in the absence of a porous medium [35]. BSRs, obtained from seismic reflection studies, indicate a negative impedance contrast between sediments that are hydrate free (but which may also contain gas) and sediments that contain gas hydrate. BSRs are parallel to the sea floor and are believed to mark the position of the base of the hydrate stability zone [35,36], although the issue is not completely resolved within the scientific community.

A significant advancement in understanding phenomena occurring within porous media comes from extensive studies using pore networks. In such an approach the real porous medium is replaced by a fictitious network of sites, representing pores, connected with bonds, representing the connecting throats. Both pores and throats can be distributed according to a specified size distribution. A large number of studies using pore networks has appeared in literature since the pioneering work by Fatt [37]. Pore networks have primarily been used to study two-phase or multiphase displacement processes in porous media. Excellent reviews have been provided by Feder [38], Sahimi [39], and Blunt and co-workers [40,41]. Among other topics, pore networks have been used to study relative permeabilities, electrical resistivities and capillary pressures, gravity and viscous forces effects on flow, the effect of spatial correlation, and wettability on transport properties (see the aforementioned reviews for an extended list of references). In recent years, pore networks have also been used to study mass transfer and phase change processes as a result of the increased computational power available. In particular, they have been used to study the liquid-to-gas phase change in porous media in processes such as solution gas drive [42,43], drying [44,45], boiling [46], and critical gas saturation during primary oil production [47,48]. Therefore, conducting studies that examine pore-scale phenomena can result in obtaining a better understanding on a fundamental level of the dissociation and/or formation of clathrate hydrates. It is the intent of this work to study clathrate hydrate dissociation using a pore-network approach and address some of the aforementioned issues at the microscale. In the current study the possible effects of hydrate dissociation kinetics are not considered.

To the authors knowledge, pore networks have only recently been applied to the study of clathrate hydrates dissociation [49,50] or formation [51] in porous media. The purpose of this work is to introduce a pore network approach for dissociation of methane hydrate and study the patterns obtained by the release of gas and their dependence on system parameters such as pore-size distribution, applied pressure difference across the network, and initial hydrate saturation.

In addition to pore networks, porous media have been represented with more realistic and sophisticated methods. A detailed discussion of the porous-media reconstruction issue can be found in the works of Adler [52] and Torquato [53,54]. Reconstruction of more realistic, three-dimensional, porous media was also coupled with chemical reactions by Bekri *et al.* [55,56].

II. PROBLEM STATEMENT

Consider a geological porous medium saturated with water and which also contains a methane hydrate phase distributed homogeneously throughout the pore space. The hydrate saturation in an oceanic porous sediment, S_H, can vary between values as low as 4–8 % and as high as 20–30 % of the pore space. The lower limit has been reported from studies at Blake Ridge [57], while the higher limit has been reported from studies at Cascadia Margin [57] (offshore Vancouver Island, Canada). Estimates for hydrate saturation can be obtained using seismic velocity models [35], resistivity [6], and chlorinity measurements [58,6]. In order to explain gas hydrate formation in geological sediments, two models that consider different gas supplies have been proposed. In the first model, methane is produced locally by an *in situ* biogenic conversion of carbon that is deposited within the hydrate stability zone [59]. In this case, hydrate formation occurs throughout the entire hydrate stability zone and results in having an almost uniform distribution of hydrate within the zone. This model can also explain the lower limit of hydrate saturation, since hydrate formation is limited by the amount of gas produced locally, which in turn is controlled by the amount of organic matter deposited in the sediments. In the second model, methane is produced below the hydrate stability zone and moves upward and into the stability zone by rising fluid [60]. This model results in creating higher hydrate saturation at the lower part of the hydrate stability zone with hydrate saturation thinning out towards the top of the formation.

For a given temperature T_{eq} and pore radius (dissociation occurs at lower temperatures or higher pressures relative to the case when no porous medium is present) corresponds to

an equilibrium pressure P_{eq}, below which hydrate dissociates. The equilibrium dissociation pressure can be calculated using a methodology based on thermodynamic principles and by applying the van der Waals–Platteeuw theory [61,31]. The hydrate remains stable within the porous medium provided the pressure in the porous medium remains above the dissociation pressure P_{eq}. Once the pressure drops below P_{eq}, the hydrate dissociates into water (if the temperature is above the freezing temperature of water) and gas. It is reported that during hydrate formation all the water inside a pore can solidify into hydrate with the exception of a thin (5–50 nm) adsorbed film that remains liquid [62]. Ice is strongly nonwetting and forms convex shapes within the pores that minimize surface area [62]. This hypothesis was also confirmed by the visualization experiments of Tohidi *et al.* [29]. Therefore, during the dissociation of the hydrate, the liquid phase is the wetting phase while the produced methane occupies the pore centers.

After the dissociation of hydrate has occurred, two steps can be identified in the subsequent processes. During the first step the gas phase (initial gas cluster) occupies a part of the pore without contacting (reaching) the pore walls. If the pressure in the gas phase P_g is higher than the surrounding liquid phase P_l in the same pore, then the gas cluster can grow, expelling liquid until $P_g = P_l$ or it reaches the pore walls. Further growth may be opposed by capillary forces at neighboring pore throats, completing the end of the first step (see Fig. 1 for a schematic). This step has a significant consequence. In the case that $P_l > P_g$ in a given pore, there is no growth of the gas phase, namely the gas phase will remain isolated in the pore, not having the ability to connect with other neighboring gas clusters. Such an event negatively affects the connectivity of the gas phase and thus the ability to produce the gas phase. This issue is examined in detail in Tsimpanogiannis *et al.* [63] for different pore geometries. It was shown in [63] that in order for gas phase growth to occur, one of the throats (connected to the pore) must have a radius, r, that satisfies the following condition:

$$r > \frac{2\gamma}{z\lambda^* RT_{eq} - P_l}, \tag{1}$$

where z is the compressibility factor, R is the gas constant, γ is the interfacial tension, and λ^* is a parameter with a value of about 6.75 and units of inverse volume.

During the second step, if the pressure in the resulting gas phase P_g is high enough to overcome the capillary threshold of at least one of the neighboring throats, it can expand until there is capillary pressure equilibrium within the system. Upon growth, the various gas clusters that result from the dissociation of the methane hydrate can coalesce and eventually form a continuous path connected to the exit. Such continuous paths enable production of the dissociated methane. Upon formation of a continuous gas path (*sample-spanning gas cluster*), the critical gas saturation S_{gc} (defined as the volume fraction of the gas phase over the entire network at the onset of bulk gas flow) is reached (see also Tsimpanogiannis and Yortsos [48] for the more general case of critical gas saturation in the presence of gravity gradients).

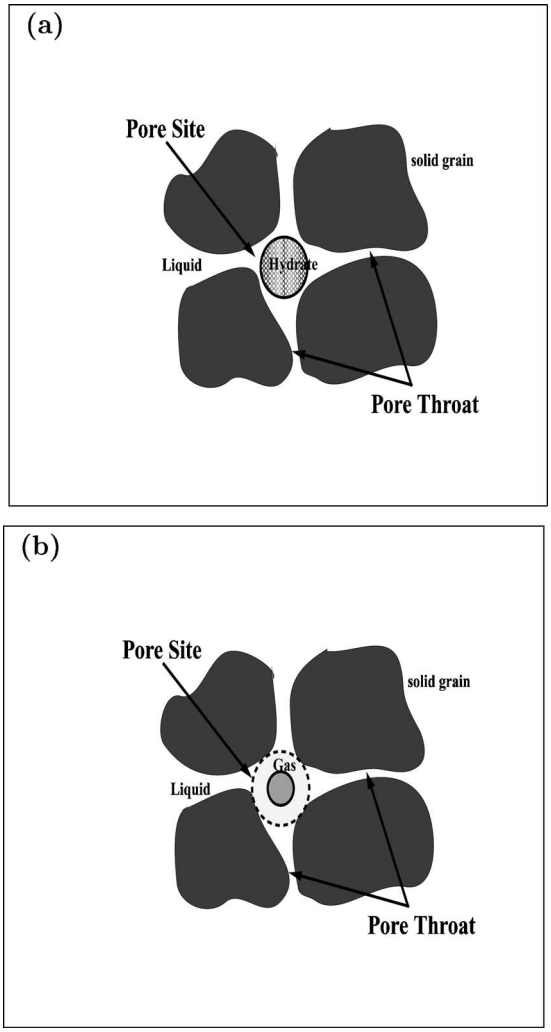

FIG. 1. Schematic of a pore site (a) showing hydrate occupied site and (b) gas occupied site (dashed line denotes gas growth at the end of the first step).

Before reaching S_{gc}, the only gas produced at the well is the amount that is dissolved at the liquid phase. After reaching S_{gc}, the amount of gas produced at the well is increased by the amount of free gas that is flowing through the interconnected gas path. Therefore, a significant increase in gas production is observed at the well after reaching S_{gc}. The critical gas saturation can also be reached in the case that the resulting initially isolated gas clusters can be mobilized through viscous and/or gravity forces and thus arrive at the production end. However, as a first approximation to the hydrate dissociation problem, gas cluster migration in response to an applied pressure gradient is not examined further here. Detailed results are to be presented in a future publication, but it is expected to be of importance, at least for large throat sizes in the network. The value of the critical gas saturation for a particular sediment determines the threshold gas saturation necessary for producing the released gas phase. During methane hydrate dissociation, in order for methane production to be possible, the production process needs to operate above the critical gas saturation (compare with primary oil production during the solution gas drive case, where the pro-

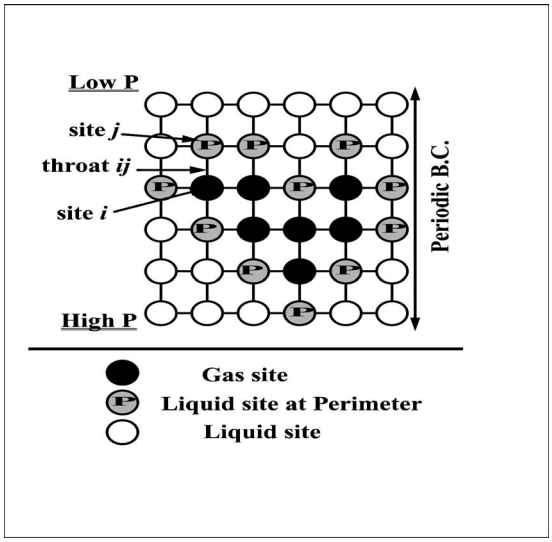

FIG. 2. Schematic of a square lattice showing gas occupied sites (denoted by black), liquid occupied sites (denoted by white), and liquid occupied sites at the outside perimeter of the gas phase (denoted by gray).

cess needs to be below S_{gc} since interest is primarily in the production of the liquid phase).

To simulate hydrate dissociation in the abscence of hydrate dissociation kinetics, a two-dimensional (2D) pore-network representation is assumed in the form of a regular lattice of size $N \times N$. In order to calculate volumes, we also assume that the network has unit length in the third dimension (see Fig. 2 for a schematic). Pores are taken to be spherical while throats are cylindrical. Both pores and throats are randomly distributed and uncorrelated with radius having values in the range $r_i \in [r^{\min}, r^{\max}]$ and $r_{ij} \in [r_*^{\min}, r_*^{\max}]$, respectively. Figure 3 shows a schematic of two pores connected with a throat. We further consider that the network has total length, L, that is given by $L=Nl$, where l is equal to

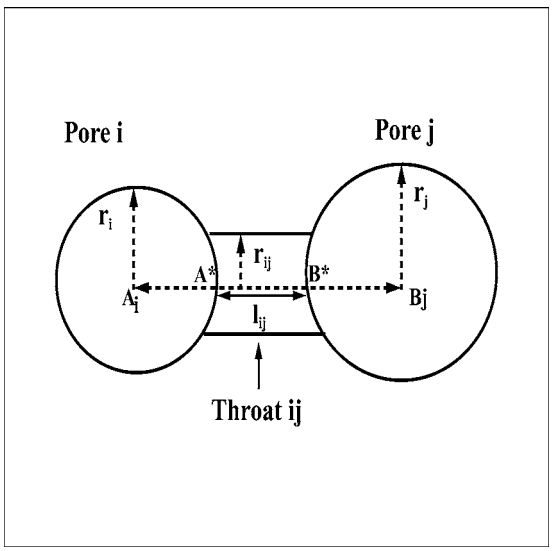

FIG. 3. Schematic of pore-network geometry showing spherical pores i and j connected with a cylindrical throat.

the distance A_iB_j between the centers of two neighboring pores. This distance is taken as $l=2r^{\max}$. Therefore, the length of the throat A^*B^* connecting pores i and j is calculated from $l_{ij}=l-(r_i+r_j)$. The porosity ϕ is calculated as the ratio of the pore volume to the total network volume, $\phi = V_p/V_{\text{total}}$. In general, both pores and throats contribute to the pore volume, $V_p=V_{\text{pores}}+V_{\text{throats}}$. For the specific geometry under consideration,

$$V_p = \sum_{i=1}^{N^2} \frac{4}{3}\pi r_i^3 + \sum_{i \neq j} \pi r_{ij}^2 l_{ij}, \tag{2}$$

where the second sum runs over the $2N(N-1)$ throats. The average radius for pores and throats can be defined as $\bar{r}_p = \langle r_i \rangle$ and $\bar{r}_t = \langle r_{ij} \rangle$, respectively. The ratio of the average pore radius to the average throat radius defines a new parameter λ ($\lambda \equiv \bar{r}_p/\bar{r}_t$). Usually in the simulations, the pores were taken to be one order of magnitude larger than the throats (i.e., $\lambda=10$). Numerical simulations have shown that approximately for $\lambda > 4$ the throat contribution to the total porosity is limited. Consequently, it is a reasonable assumption to consider that the lattice pores provide the storage capacity of the network, while the throats connecting neighboring pores provide the resistance to flow, without contributing to the storage capacity.

Application of the methodology to a more realistic geometry of the porous medium is straightforward but more tedious. For example, triangular or square throats, in addition to affecting porosity, can provide for additional liquid remaining at the corners (also known as "thick" film or "corner" film) after invasion of the nonwetting (gas) phase (compared to no liquid remaining after invasion in cylindrical throats, other than a very thin film which can carry negligible flow). This can result in better connectivity and flow of the liquid phase (see also the work of Yiotis *et al.* [64] for the effect of "thick" films for the case of drying). Periodic boundary conditions are used in the directions perpendicular to the inlet and/or outlet direction.

Initially all the lattice pores are filled with water, which is considered as the "defending" fluid during the simulations. The hydrate saturation in the lattice is set with pores occupied at random. This is done by using an ordinary percolation approach [65]. In this study, we do not take into account the adsorbed thin water film that does not solidify (see the discussion in the early part of the current section). However, relaxing this assumption is straightforward. To begin the calculation the pressure P is lowered instantaneously at one side of the network to the value P_{low}, while keeping the pressure of the other side fixed at P_{high}. To solve for the resulting pressure field we assign conductances to each pore and throat using a modified form of Poiseuille's law. The flow rate Q flowing through the throat ij (connecting pores i, j) is given by

$$Q_{ij} = g_{ij} \Delta P_{ij}, \tag{3}$$

where ΔP_{ij} is the pressure drop across throat ij, and the conductance g_{ij} is defined as follows:

$$g_{ij} = \frac{\pi r_{ij}^4}{8\mu_l l_{ij}}, \tag{4}$$

where μ_l is the liquid viscosity, l_{ij} is the length of the throat ij, and r_{ij} is the radius of throat r_{ij}.

If we assume an incompressible liquid phase and apply volume conservation at each pore we obtain

$$\sum_j Q_{ij} = 0, \tag{5}$$

where the sum over the index j runs over all pores connected to pore i. The index i runs over all pores that are internal. This results in a system of linear algebraic equations which, when solved, gives the pressure at each pore. In matrix notation we can write

$$\underline{\underline{G}} \cdot \underline{\Delta P} = \underline{b}, \tag{6}$$

where $\underline{\underline{G}}$ is a sparse matrix that contains the conductances, $\underline{\Delta P}$ is a vector that contains the unknown pressure differences, and $\underline{b}$ is a source vector which is essentially zero everywhere except the inlet, outlet, and interface throats [66]. The solution of the system can be obtained using a biconjugate gradient method or a successive over-relaxation (SOR) method [67].

Once the pressure field is obtained, we examine whether dissociation can take place. Each hydrate cluster in the network is identified using the Hoshen-Koppelman algorithm [68]. Once the perimeter of each hydrate cluster is determined, we examine if there is a hydrate pore that has a neighboring pore with liquid pressure lower than P_{eq}. In that case, the hydrate in the considered pore is dissociated (in addition to all the other hydrate pores belonging to the same hydrate cluster). After all the hydrate clusters in the network are examined for dissociation, we then proceed to the next step and consider the possible growth of the resulting gas phase clusters. For all the gas clusters, if the pressure in the gas phase P_g is high enough, the gas phase will start advancing. This process is done as follows: All perimeter pores j that contain liquid and are adjacent to the gas cluster i are identified (see also the schematic of Fig. 2). An invasion threshold Π_{ij} is assigned to each one of them given by

$$\Pi_{ij} \equiv P_c^{ij} + P_l^j, \tag{7}$$

where P_l^j is the liquid pressure of pore j and P_c^{ij} is the capillary pressure of the throat that connects the pore j with the gas cluster pore i. A gas cluster will grow if the pressure in the gas phase satisfies

$$P_g > \Pi_{ij}. \tag{8}$$

Among all perimeter pores, the pore j with the *lowest* invasion threshold Π_{ij} will be invaded. In such a process the amount of gas in a gas cluster remains constant, while the total volume of the gas cluster, V_g, increases by adding the volume V_s^j of the newly invaded pore and thus lowering the pressure. The new pressure can be obtained through the modified ideal gas law

$$P_g = \frac{z n_g R T_g}{V_g}, \tag{9}$$

where subscript g denotes the gas phase, n_g the number of methane gas moles, which remains constant for a gas cluster as long as no coalescence with other gas clusters occurs, and $T_g = T_{\text{eq}}$ since we consider isothermal dissociation. This process is to be repeated until eventually $P_g < \Pi_{ij}$ or the gas phase of a given cluster reaches the exit, and for all the different gas clusters in the network. In case, during the growth phase of a gas cluster, the cluster reaches the exit and the gas pressure P_g is higher than $(P = P_{\text{low}})$, then the gas cluster is completely removed from the network and the pressure field is recalculated. The aforementioned process is similar to invasion percolation [69], however, the invading phase (gas) growth occurs at multiple invading fronts. As discussed in more detail in the next section, depending on the throat size distribution, this process can produce a variety of gas patterns, ranging from completely isotropic patterns (at small throat sizes) to fingering patterns (at large throat sizes).

In both cases of dissociation and gas cluster growth, we start at the side where pressure reduction occurs, since dissociation and growth phenomena are expected to appear there first.

III. RESULTS

A series of numerical simulations were conducted with lattices of various sizes. Typical parameter values used corresponding to methane dissociation are $T_{\text{eq}} = 283.2$ K, $P_{\text{eq}} = 69.5 \times 10^5$ Pa, $\mu_l = 10^{-3}$ Pa s, and $\rho_H = 913.0$ Kg/m^3. For the above conditions, we estimate that the compressibility factor is approximately $z = 0.85$ [70].

Here, it would be useful to define the terms *narrow* and *wide* throat size distributions, which are used in the remaining part of this section. Consider a throat size distribution such that $r_{ij} \in [r_*^{\min}, r_*^{\max}]$ and further define the ratio $\beta \equiv r_*^{\max}/r_*^{\min}$. A throat size distribution is called *narrow* if $\beta \leqslant 10$. A throat size distribution is called *wide* if $\beta \gg 10$.

Figure 4 shows the effect of a *narrow* throat size distribution (with $\beta = 10$) on the growth of gas phase clusters after hydrate dissociation occurring in a 200×200 lattice. Figure 4(a) shows the initial methane hydrate distribution in the network for $S_H^o = 0.02$. A lower value of hydrate saturation was selected here for better visualization of the patterns. The pressure field was solved for a dimensionless $\Delta P_D = (P_{\text{high}} - P_{\text{low}})/P_{\text{high}} = 0.8$ across the lattice corresponding to $P_{\text{high}} = 76.45 \times 10^5$ Pa and $P_{\text{low}} = 15.29 \times 10^5$ Pa. The pressure drop is along the vertical axis (low pressure occurs at the top of the network and high pressure at the bottom). In the figure caption the calculated values of absolute permeability, k, are also reported. For the reported values of the absolute permeability the following assumption is made: The gas phase is considered immobile, essentially acting as if blocking the pore space. After making this assumption, we can consider that only the liquid phase is present; therefore, the absolute permeability can be calculated. In Figs. 4(b)–4(e) the solid lines denote the transition point within the lattice, going from dissociated to nondissociated hydrate. As can be seen, disso-

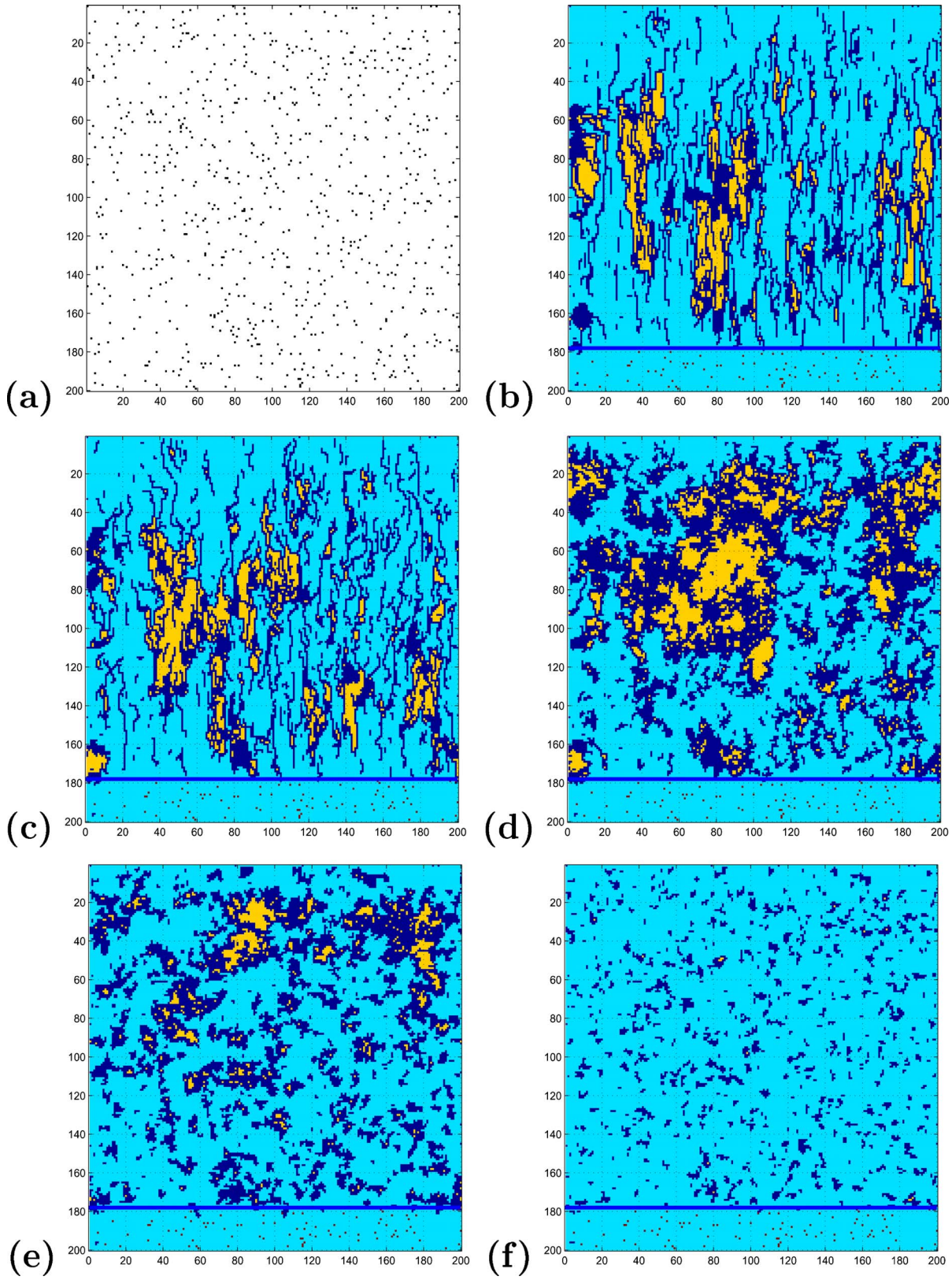

FIG. 4. (Color online) The effect of a narrow throat size distribution (with $\beta=10$) on obtained patterns in a 200×200 lattice. (a) Initial hydrate distribution in the lattice (shown in black). Distribution of gas (shown in dark blue), liquid (shown in light blue), trapped liquid (shown in yellow), and nondissociated hydrate (shown in red) for $S_H^o=0.02$, $\phi=0.15$, $\Delta P_D=0.8$ [$P_{\text{high}}=76.45\times10^5$ Pa (bottom of network), $P_{\text{low}}=15.29\times10^5$ Pa (top of network)], and throat sizes, r_{ij}, in the following range: (b) $10^{-5}-10^{-4}$ m ($k=2.44\times10^{-10}$ m^2); (c) $10^{-6}-10^{-5}$ m ($k=2.44\times10^{-12}$ m^2); (d) $10^{-7}-10^{-6}$ m ($k=2.44\times10^{-14}$ m^2); (e) $10^{-8}-10^{-7}$ m ($k=2.44\times10^{-16}$ m^2); (f) $10^{-9}-10^{-8}$ m ($k=2.44\times10^{-18}$ m^2).

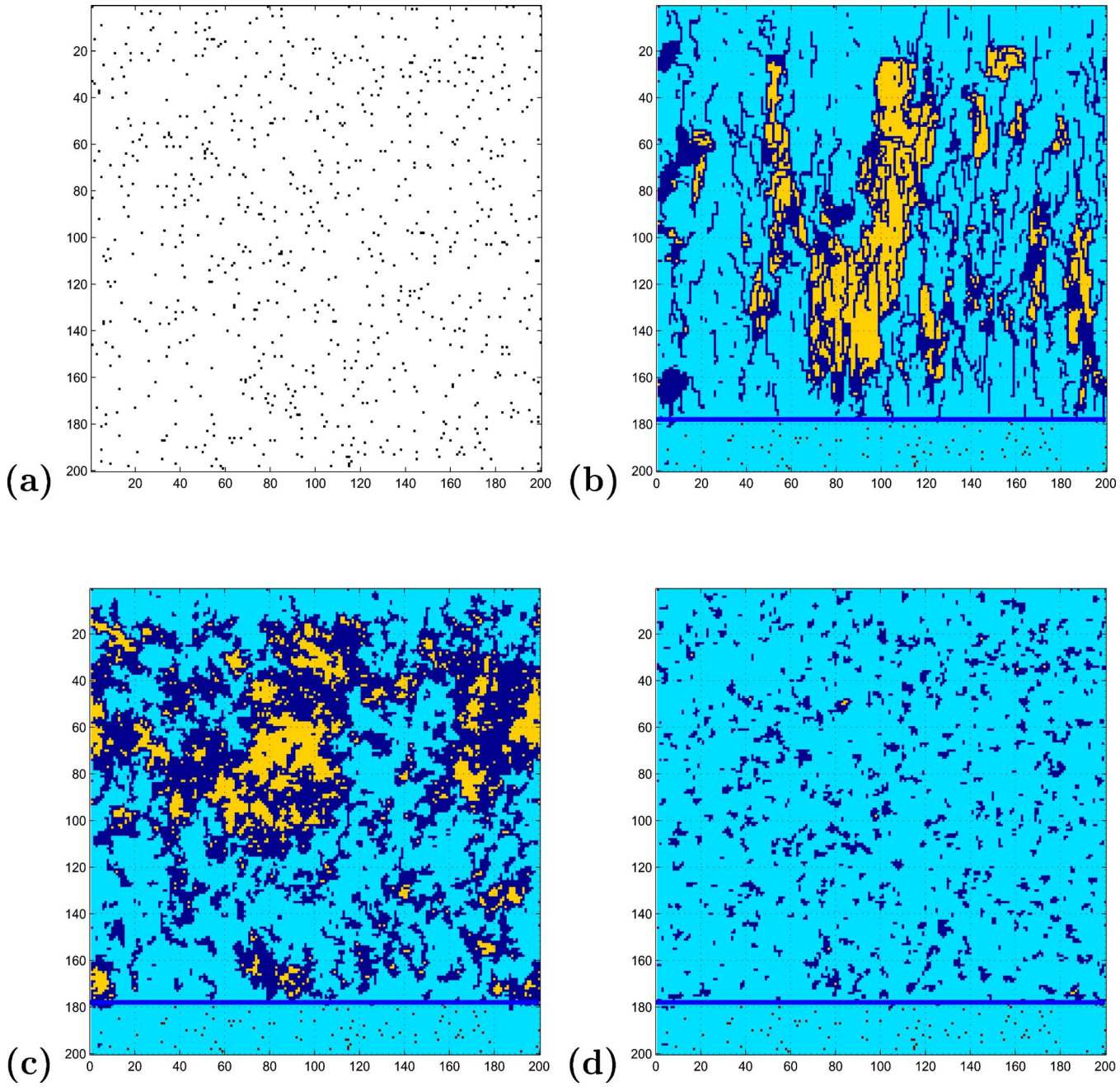

FIG. 5. (Color online) The effect of a wide throat size distribution on obtained patterns in a 200×200 lattice. (a) Initial hydrate distribution in the lattice (shown in black). Distribution of gas (shown in dark blue), liquid (shown in light blue), trapped liquid (shown in yellow), and nondissociated hydrate (shown in red) for $S_H^o=0.02$, $\Delta P_D=0.8$ [$P_{\text{high}}=76.45\times10^5$ Pa (bottom of network), $P_{\text{low}}=15.29\times10^5$ Pa (top of network)], and throat sizes, r_{ij}, in the following range: (b) $10^{-9}-10^{-4}$ m, $\beta=10^5$ ($\phi=0.1332$, $k=1.81\times10^{-10}$ m^2); (c) $10^{-9}-10^{-6}$ m, $\beta=10^3$ ($\phi=0.1334$, $k=1.82\times10^{-14}$ m^2); (d) $10^{-9}-10^{-8}$ m, $\beta=10$ ($\phi=0.1478$, $k=2.44\times10^{-18}$ m^2).

ciation does not take place over a zone of an approximate length of 20 pores.

For the case of very small throat sizes [Fig. 4(f)], there is essentially very little or no growth of the gas clusters. That is because the dominant term in the invasion threshold, Π_{ij}, is the throat capillary pressure, P_c^{ij}, which is higher than the gas pressure P_g, thus inhibiting any further growth. For the case of medium throat sizes [Figs. 4(d) and 4(e)], there is growth of the gas clusters and the resulting growth patterns are similar to invasion percolation corresponding to multiple invading fronts. Here, the contribution of the throat capillary pressure and the liquid pressure to the invasion threshold is balanced, resulting in invasion patterns that have more or less isotropic structure. However, as we go toward larger throat sizes [Figs. 4(b) and 4(c)] we observe the formation of single "fingers," made up of collections of fractal blobs that resemble the patterns produced by invasion percolation in a destabilizing gradient (discussed in detail by Frette *et al.* [71] and Meakin *et al.* [72]). In this case the dominant term in the invasion threshold is the liquid pressure P_l^j, which, of course,

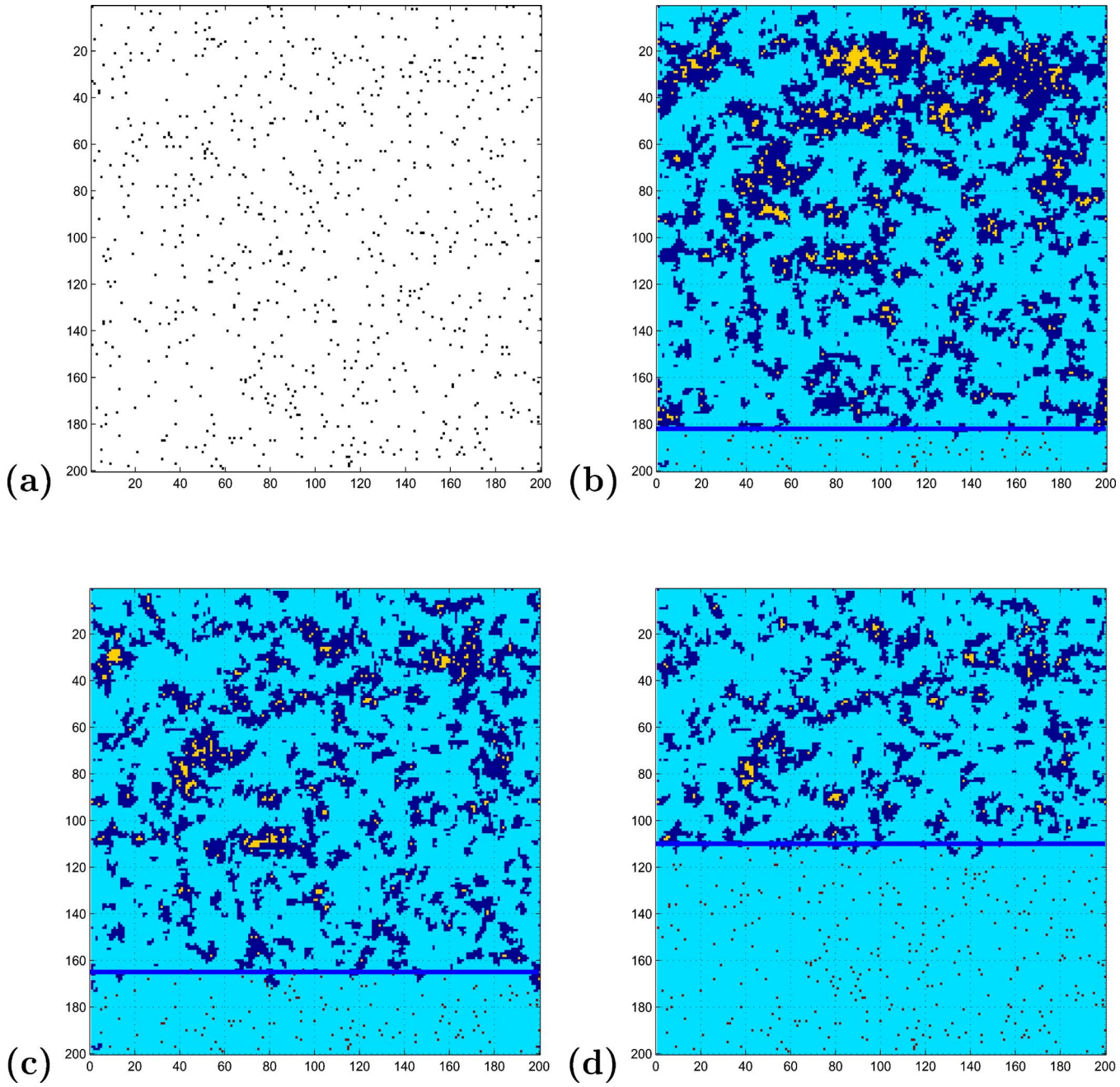

FIG. 6. (Color online) The effect of ΔP_D [$P_{\text{high}}=76.45\times10^5$ Pa (bottom of network)] on obtained patterns in a 200×200 lattice. (a) Initial hydrate distribution in the lattice (shown in black). Distribution of gas (shown in dark blue), liquid (shown in light blue), trapped liquid (shown in yellow) and nondissociated hydrate (shown in red) for $S_H^o=0.02$, and throat sizes, r_{ij}, in the range $10^{-8}-10^{-7}$ m, $\phi=0.15$, and for the following: (b) $\Delta P_D=0.9$, $P_{\text{low}}=7.645\times10^5$ Pa, $k=2.40\times10^{-16}$ m^2; (c) $\Delta P_D=0.5$, $P_{\text{low}}=38.225\times10^5$ Pa, $k=2.57\times10^{-16}$ m^2; (d) $\Delta P_D=0.2$, $P_{\text{low}}=61.160\times10^5$ Pa, $k=3.09\times10^{-16}$ m^2. P_{low} is located at the top of the network.

exhibits a gradient and thus results in a gradient in the invasion threshold, Π_{ij}.

At very small throat sizes [Figs. 4(e) and 4(f)] the gas phase is neither connected nor can be mobilized easily, thus hindering its production (gas phase saturation is below the critical gas saturation). Extensive gas phase interconnection exists for medium and large throat sizes [Figs. 4(b)–4(d)], thus allowing for gas production. For large throat sizes [Figs. 4(b) and 4(c)], the gas phase is in the form of isolated clusters which can be easily mobilized.

Figure 5 shows the effect of a *wide* throat size distribution on the growth of the gas phase clusters after hydrate dissociation occurring in a 200×200 lattice and a dimensionless $\Delta P_D=0.8$ across the lattice. Figure 5(a) shows the initial methane clathrate distribution in the network for $S_H^o=0.02$. Again in the presence of large throat sizes fingering patterns are obtained (indicating P_l^j to be dominant term), while in the absence of large throat sizes isotropic patterns are obtained (indicating P_c^{ij} to be the dominant term).

Figure 6 shows the effect of the imposed ΔP_D across the

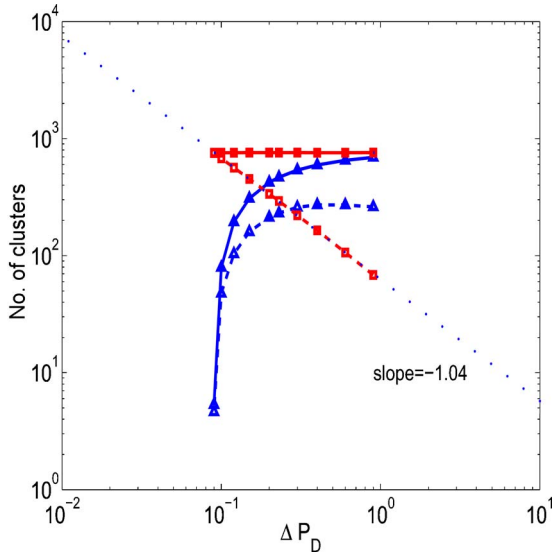

FIG. 7. (Color online) The number of clusters (denoted by triangles for gas and square for hydrate) as a function of ΔP_D for a 200×200 lattice, averaged over 100 realizations, $S_H^o=0.02$, $\phi=0.15$, and throat sizes, r_{ij}, in the range $10^{-8}-10^{-7}$ m. Solid lines correspond to the beginning of the process (defined before dissociation for the hydrate or before growth for the gas clusters). Dashed lines correspond to the end (defined after dissociation ends for the hydrate or after growth ends for the gas clusters).

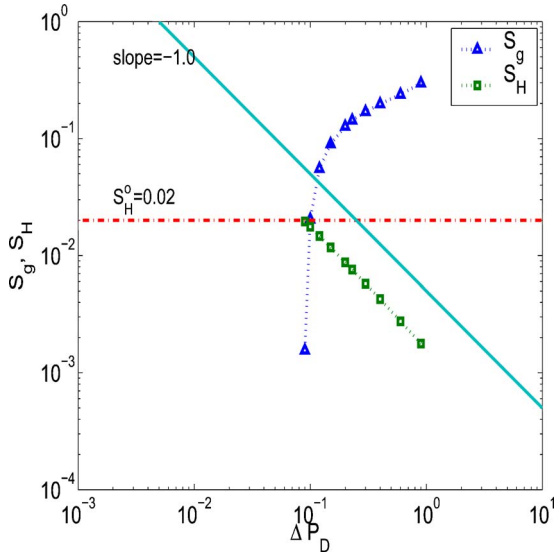

FIG. 8. (Color online) The gas saturation S_g (triangles) and the hydrate saturation S_H (squares) as a function of ΔP_D ($P_{\text{high}}=76.45\times10^5$ Pa and various P_{low}) for a 200×200 lattice, averaged over 100 realizations, $S_H^o=0.02$, $\phi=0.15$, and throat sizes, r_{ij}, in the range $10^{-8}-10^{-7}$ m. The horizontal dashed-dotted line denotes the initial saturation, while the solid line denotes the theoretical slope equal to −1.

network on the patterns formed for a 200×200 lattice, with $S_H^o=0.02$, and throat sizes in the range $10^{-8}-10^{-7}$ m. As mentioned earlier, higher ΔP_D leads to higher gas saturation in the system (more liquid displaced out of the system). As also can be seen, if ΔP_D increases, this results in lowering the width of the undissociated hydrate zone, L_H. Note that $L_T=L_g+L_H$, where L_g is the width of the zone occupied by gas-liquid and L_T is the total length of the lattice. The width of the undissociated hydrate zone, L_H, can be calculated using the following expression:

$$L_H=\frac{P_{\text{high}}-P_{\text{eq}}}{\Delta P}L_T. \tag{10}$$

Figure 7 shows on a log-log plot the number of hydrate clusters, N_{HC}, before dissociation occurs (denoted by squares that are connected with a solid line) and after the end of dissociation (denoted by squares that are connected with a dashed line). The depicted results are averages over 100 realizations. From the simulations, we obtain the following relation for the number of undissociated hydrate clusters: $N_{\text{HC}}\sim\Delta P^{-1.04}$ (see dotted line in the figure which shows the best-fit line). The exponent is very close to the theoretically predicted value of −1. Figure 7 also shows the number of gas clusters, N_{gC}, before any gas growth occurs (denoted by triangles that are connected with a solid line) and after gas cluster growth is completed (denoted by triangles that are connected with a dashed line). An asymptotic value is expected to be obtained for high ΔP_D corresponding to the case of all hydrate clusters being dissociated. Similarly, an asymptotic value is expected to be obtained for low ΔP_D corresponding to the case of no hydrate clusters being dissociated (case of no practical interest). From the figure we can observe that at high ΔP_D, the initial number of hydrate and gas clusters are very close, indicating that an increase in hydrate dissociation occurs. However, at low ΔP_D, a significant difference occurs, indicating limited hydrate dissociation. Essentially no dissociation (or very limited) occurs below $\Delta P_D=0.1$. Additionally, at high ΔP_D there is a difference between the number of gas clusters before and after expansion is allowed to take place (indicating that significant cluster coalescence takes place). The effect of coalescence becomes less significant at lower values of ΔP_D.

Figure 8 shows on a log-log plot the gas saturation S_g and the hydrate saturation S_H as a function of ΔP_D for a 200×200 lattice, averaged over 100 realizations, with $S_H^o=0.02$ and throat sizes, r_{ij}, in the range $10^{-8}-10^{-7}$ m. As ΔP_D increases the gas saturation increases as expected, since there is higher driving force for the phase change and gas growth process in the system. We observe the following scaling, valid for lower values of S_H: $S_g\sim\Delta P^{0.50}$. The hydrate saturation S_H follows very closely the expected scaling $S_H\sim\Delta P^{-1.0}$ for values of ΔP_D higher than 0.1, while essentially no dissociation occurs for values of ΔP_D lower than 0.1.

The variation of the capillary number Ca (defined for the entire network) as a function of ΔP_D, for the same realizations as above, is shown on a log-log scale in Fig. 9. The capillary number expresses the ratio of viscous to capillary forces and is defined as $\text{Ca}=q\mu/\gamma$, where q is the flowing liquid velocity, μ is the liquid viscosity, and γ is the interfacial tension. The dashed-dotted line depicts the best-fit line (with a slope equal to 0.76) calculated using data for $\Delta P_D>0.2$.

Figure 10 shows the variation of the absolute permeability k, at the end of the gas phase growth, as a function of ΔP_D

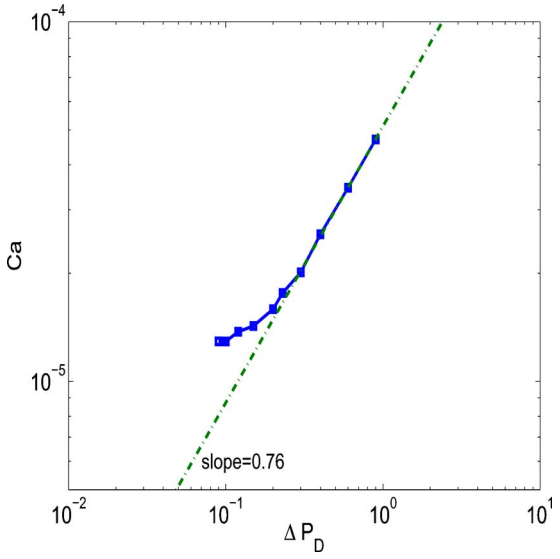

FIG. 9. (Color online) The capillary number Ca as a function of ΔP_D ($P_{\text{high}}=76.45\times10^5$ Pa and various P_{low}) for a 200×200 lattice, averaged over 100 realizations, $S_H^o=0.02$, and throat sizes, r_{ij}, in the range $10^{-8}-10^{-7}$ m.

and for the same realizations as above. Recall that in this study the gas phase is considered immobile. Therefore, the presence of gas in the pore space is equivalent to pore blocking. Consequently, higher ΔP_D results in higher hydrate dissociation and further gas growth, which in turn results in increased gas in the system and finally lower permeability as shown in the figure. By combining Darcy's law and the definition for the capillary number we can obtain the following relation for permeability:

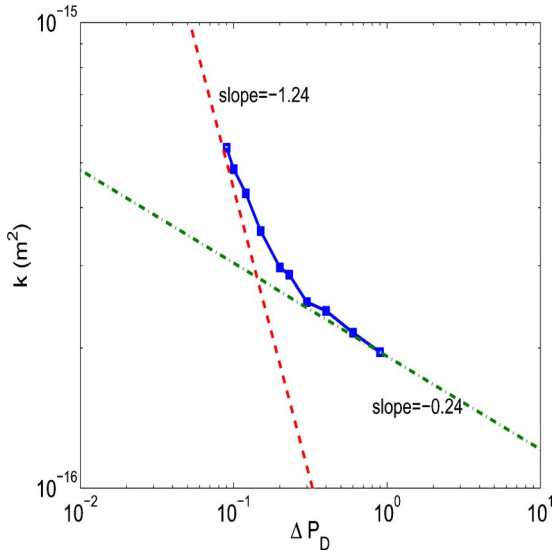

FIG. 10. (Color online) The absolute permeability k of the pore network at the end of gas phase growth as a function of ΔP_D ($P_{\text{high}}=76.45\times10^5$ Pa and various P_{low}) for a 200×200 lattice, averaged over 100 realizations, $S_H^o=0.02$, and throat sizes, r_{ij}, in the range $10^{-8}-10^{-7}$ m.

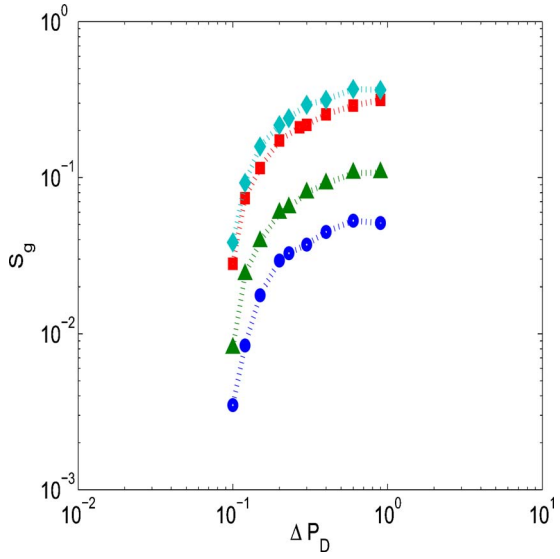

FIG. 11. (Color online) The gas saturation S_g as a function of ΔP_D ($P_{\text{high}}=76.45\times10^5$ Pa and various P_{low}) for different initial hydrate saturations S_H^o ($S_H^o=0.01$, circles; $S_H^o=0.02$, triangles; $S_H^o=0.03$, squares; $S_H^o=0.04$, diamonds) for a 50×50 lattice, averaged over 50 realizations and throat sizes, r_{ij}, in the range $10^{-8}-10^{-7}$ m.

$$k \sim \frac{\text{Ca}L_H}{\Delta P_D}. \tag{11}$$

As discussed earlier, $L_H\sim\Delta P^{\alpha}$, where $\alpha=-1$ when the dissociation zone depends on ΔP [see Eq. (10)] and $\alpha=0$ when hydrate dissociates in the entire network. Recall also that we have found $\text{Ca}\sim\Delta P^{0.76}$. Therefore, we obtain $k\sim\Delta P^{\alpha-0.24}$. Figure 10 shows the two resulting asymptotes. The dashed-dotted line corresponds to the case when $\alpha=0$ (complete hydrate dissociation in the system) and the dashed line corresponds to the case when $\alpha=-1$. As can be seen, the numerical simulations follow reasonably well the asymptotic lines for the cases of high and low $\Delta P's$ with deviation in between.

The effect of the initial hydrate saturation S_H in the network on the resulting gas saturations S_g, as a function of ΔP_D, is shown in a log-log scale in Fig. 11. The results are for a 50×50 lattice, averaged over 50 realizations and throat sizes, r_{ij}, in the range $10^{-8}-10^{-7}$ m. As expected, increasing the initial hydrate saturation yields higher gas saturations.

Figure 12 shows the effect of the initial hydrate saturation S_H in the network on the normalized number of gas clusters in the network (normalized with the initial number of hydrate clusters). Higher initial hydrate saturation results in a smaller number of clusters at the end of the process due to coalescence of gas clusters. Note that coalescence results in better connectivity of the gas phase, and therefore, acts as a promoter of the gas phase production.

IV. DISCUSSION

While this work provides a first attempt to simulate at the pore-network level phenomena occurring during hydrate dissociation, additional work is needed for obtaining a better

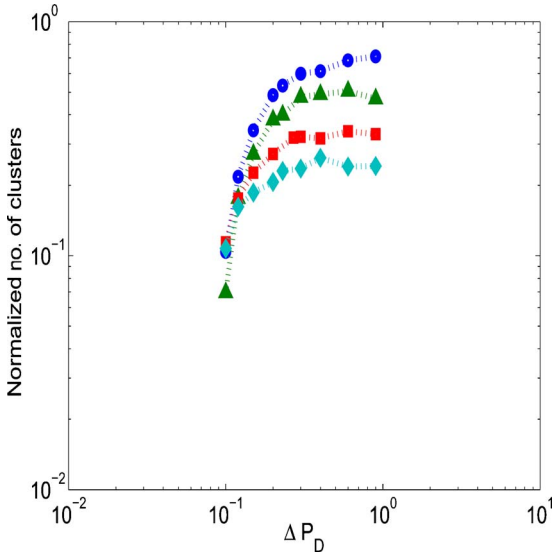

FIG. 12. (Color online) The normalized number of gas clusters as a function of ΔP_D ($P_{\text{high}}=76.45\times10^5$ Pa and various P_{low}) for different initial hydrate saturations S_H^o ($S_H^o=0.01$, circles; $S_H^o=0.02$, triangles; $S_H^o=0.03$, squares; $S_H^o=0.04$, diamonds), for a 50×50 lattice, averaged over 50 realizations and throat sizes, r_{ij}, in the range $10^{-8}-10^{-7}$ m.

understanding of the problem. In this section, some directions that need further investigation are pointed out.

A. Heat effects

Here we considered the isothermal dissociation of methane hydrate. However, the methane dissociation process is endothermic. Ruef *et al.* [73] reported that the average enthalpy of dissociation is 429.66 KJ/Kg. Inclusion of the heat effects at the pore-network scale for the hydrate dissociation problem is currently under investigation and results will be reported in a future publication.

B. Hydrate dissociation kinetics

In this work we considered the case where *instantaneous* dissociation occurs. Namely, for each hydrate cluster, we examine if there is a hydrate site that has a neighboring liquid occupied site with pressure lower than P_{eq}. In that case the hydrate in the considered site is dissociated (in addition to all the other hydrate sites belonging to the same hydrate cluster). This assumption may be acceptable for the case where we have small hydrate clusters (usually that is the case when the hydrate saturation, S_H, is low); however, it is expected to be inaccurate for larger clusters (that is the case with higher S_H). In that case, one needs to incorporate dissociation kinetics into the model. Such an effort was undertaken by Tsimpanogiannis *et al.* [74] who examined the case of a pore network fully saturated with hydrate and proceeded to solve the problem using the kinetic model of Kim *et al.* [75]. A next step could be the coupling of the current and the aforementioned work to provide a unified approach for the entire range of hydrate saturations. Note that the kinetic model of Kim *et al.* [75] was developed for a batch-reactor system and in the absence of porous media.

C. Experimental work

A large number of experimental works exist addressing issues related mostly to thermodynamics. A significant lesser amount of experimental work exists of studies in porous media such as sand packs, bead packs, and cores. While such studies are extremely useful, they do not allow for direct visualization of the phenomena occurring at the pore level. To achieve this goal, experiments in 2D transparent networks are needed. Typical examples include Hele-Shaw cells, 2D bead packs, and etched networks on glass or poly-methyl-meth-acrylate. The only known visualization work on hydrates using two-dimensional transparent glass micromodels is the one by Tohidi *et al.* [29]. Using such experiments, one can identify the various steps of the dissociation (or formation) process, which then can be incorporated in the numerical simulators, making them more realistic. These types of experiments can also be used for code verification.

D. Applied pressure difference

Throughout this work, emphasis was placed on higher values of applied pressure difference across the network. That resulted in obtaining a variety of gas patterns depending on the throat size distribution. At the field scale, higher values of pressure difference are expected to exist very close to the producing well; however, when far from the well bore the used values may be somewhat unrealistic. It is, therefore, essential to examine in detail the case where dissociation occurs in the network for a very small pressure difference across the network (with the pressure below the dissociation pressure). The role of critical gas saturation during methane production and its scaling with various parameters of the system is considered in detail by Tsimpanogiannis *et al.* [76] for the aforementioned case.

V. CONCLUSIONS

This work resulted in two main contributions that enhance the understanding of hydrate dissociation within a porous medium. First the concept of the critical gas saturation, S_{gc}, during methane hydrate dissociation was introduced. The importance of operating above the critical value for methane production in the field scale was pointed out. Then a pore-network model, based on invasion percolation theory, was introduced to simulate the isothermal dissociation of methane hydrates in porous media. The effects of pore-size distribution, applied pressure difference across the network, and initial hydrate saturation on the obtained patterns were examined.

It was demonstrated that, depending on the throat sizes of the sediments, different gas patterns can be obtained. In the case that capillary forces are dominant (e.g., narrow distributions of small throats), isotropic and fractal gas patterns are obtained. At low initial hydrate saturations, the gas phase is isolated in small clusters that cannot be mobilized easily (unless very close to the production well), thus hindering gas

production (process operating below the critical gas saturation). On the other hand, when viscous forces are dominant (e.g., large throats or wide distributions), fingering types of patterns are obtained, with increased gas phase connectivity, which allow gas production (process operating above the critical gas saturation).

In this study, the focus was on lower initial hydrate saturation and the effect it has on gas patterns and the critical gas saturation. It is expected that for higher initial hydrate saturations increased gas connectivity can be achieved. Therefore, gas production may be possible even in the case of small throat sizes, as in oceanic sediments. Several directions which merit further investigations in the future were also pointed out.

ACKNOWLEDGMENTS

This work was supported by LDRD-DR 20030059DR, the contribution of which is gratefully acknowledged. We also gratefully acknowledge fruitful discussions with Professor Y. C. Yortsos (University of Southern California) and Dr. D. Hickmott (LANL, EES-6) for carefully reviewing the manuscript.

[1] J. W. Wilder, K. Seshardi, and D. H. Smith, Langmuir **17**, 6729 (2001).
[2] P. Englezos, Ind. Eng. Chem. Res. **32**, 1251 (1993).
[3] E. D. Sloan, Energy Fuels **12**, 191 (1998).
[4] S. Thomas and R. A. Dawe, Energy **28**, 1461 (2003).
[5] W. L. Mao and H. K. Mao, Proc. Natl. Acad. Sci. U.S.A. **101**, 708 (2004).
[6] B. A. Buffet, Annu. Rev. Earth Planet Sci. **28**, 477 (2000).
[7] K. A. Kvenvolden, Proc. Natl. Acad. Sci. U.S.A. **96**, 3420 (1999).
[8] A. V. Milkov, Earth-Sci. Rev. **66**, 183 (2004).
[9] K. A. Kvenvolden, Rev. Geophys. **31**, 173 (1993).
[10] P. G. Brewer, C. Friederich, E. T. Peltzer, and F. M. Orr, Jr., Science **284**, 943 (1999).
[11] C. Marchetti, Clim. Change **1**, 59 (1977).
[12] S. Hirohama, Y. Shimoyama, A. Wakabayashi, S. Tatsuta, and N. Nishida, J. Chem. Eng. Jpn. **29**, 1014 (1996).
[13] K. Ohgaki, K. Takano, H. Sangawa, T. Matsumara, and S. Nakano, J. Chem. Eng. Jpn. **29**, 478 (1996).
[14] W. Rice, ASME J. Energy Resour. Technol. **125**, 253 (2003).
[15] G. T. Mac Donald, Clim. Change **16**, 247 (1990).
[16] C. A. Koh, R. E. Westacott, and W. Zhang, Fluid Phase Equilib. **194-197**, 143 (2002).
[17] C. A. Koh, Chem. Soc. Rev. **31**, 157 (2002).
[18] E. D. Sloan, *Clathrate Hydrates of Natural Gases*, 2nd ed. (Dekker, New York, 1998).
[19] E. D. Sloan, Nature (London) **426**, 353 (2003).
[20] Y. F. Makogon, *Hydrates of Hydrocarbons* (Pennwell, Tulsa, 1997).
[21] Y. P. Handa and D. Stupin, J. Phys. Chem. **96**, 8599 (1992).
[22] T. Uchida, T. Ebinuma, and T. Ishizaki, J. Phys. Chem. B **103**, 3659 (1999).
[23] T. Uchida, T. Ebinuma, S. Takeya, J. Nagao, and H. Narita, J. Phys. Chem. B **106**, 820 (2002).
[24] J. W. Wilder, K. Sheshardi, and D. H. Smith, J. Phys. Chem. B **105**, 9970 (2001).
[25] K. Sheshardi, J. W. Wilder, and D. H. Smith, J. Phys. Chem. B **105**, 2627 (2001).
[26] D. H. Smith, J. W. Wilder, and K. Sheshardi, AIChE J. **48**, 393 (2002).
[27] R. Anderson, M. Llamendo, B. Tohidi, and R. W. Burgass, J. Phys. Chem. B **107**, 3500 (2003).
[28] R. Anderson, M. Llamendo, B. Tohidi, and R. W. Burgass, J. Phys. Chem. B **107**, 3507 (2003).
[29] B. Tohidi, R. Anderson, M. B. Clennell, R. W. Burgass, and A. B. Biderkab, Geology **29**, 867 (2001).
[30] M. A. Clarke, M. Pooladi-Darvish, and P. R. Bishnoi, Ind. Eng. Chem. Res. **38**, 2485 (1999).
[31] J. B. Klauda and S. I. Sandler, Ind. Eng. Chem. Res. **40**, 4197 (2001).
[32] A. J. Bolton, A. J. Maltman, and Q. Fisher, Mar. Pet. Geol. **17**, 657 (2000).
[33] Y. Yang and A. C. Aplin, Mar. Pet. Geol. **15**, 163 (1998).
[34] I. N. Tsimpanogiannis and P. C. Lichtner, J. Petr. Sci. Eng. (2006) (to be published).
[35] P. Henry, M. Thomas, and M. B. Clennell, J. Geophys. Res. **104**, 23005 (1999).
[36] C. Ecker, J. Dvorkin, and A. M. Nur, Geophysics **65**, 565 (2000).
[37] I. Fatt, Trans. AIME **207**, 144 (1956).
[38] J. Feder, *Fractals* (Plenum, New York, 1988).
[39] M. Sahimi, *Flow and Transport in Porous Media and Fractured Rock: From Classical Methods to Modern Approach* (VHC, Weinheim, 1995).
[40] M. J. Blunt, SPEJ **2**, 70 (1997).
[41] M. J. Blunt, M. D. Jackson, M. Piri, and P. H. Valvante, Adv. Water Resour. **25**, 1069 (2002).
[42] X. Li and Y. C. Yortsos, AIChE J. **41**, 214 (1995).
[43] A. Dominguez, S. Bories, and M. Prat, Int. J. Multiphase Flow **26**, 1951 (2001).
[44] A. G. Yiotis, A. K. Stubos, A. G. Boudouvis, and Y. C. Yortsos, Adv. Water Resour. **24**, 439 (2001).
[45] M. Prat and F. Bouleux, Phys. Rev. E **60**, 5647 (1999).
[46] C. Satik and Y. C. Yortsos, ASME J. Heat Transfer **118**, 455 (1996).
[47] S. R. McDougall and K. S. Sorbie, Pet. Geosci. **5**, 229 (1999).
[48] I. N. Tsimpanogiannis and Y. C. Yortsos, J. Colloid Interface Sci. **270**, 388 (2004).
[49] I. N. Tsimpanogiannis and P. C. Lichtner, EOS Trans. Am. Geophys. Union **84**, OS51B-0848 (2003).
[50] I. N. Tsimpanogiannis and P. C. Lichtner SPE Annual Technical Conference and Exhibition, Houston, TX, 2004, Paper SPE 90743.
[51] Q. Kang, I. N. Tsimpanogiannis, D. Zhang, and P. C. Lichtner, Fuel Process. Technol. **86**, 1647 (2005).
[52] P. M. Adler, *Porous Meida: Geometry and Transports*

(Butterworth-Heinemann, New York, 1992).
[53] S. Torquato, *Random Heterogeneous Materials: Microstructure and Macroscopic Properties* (Springer-Verlag, New York, 2002).
[54] S. Torquato, Annu. Rev. Mater. Res. **32**, 77 (2002).
[55] S. Bekri, J. F. Thovert, and P. M. Adler, Chem. Eng. Sci. **50**, 2765 (1995).
[56] S. Bekri, J. F. Thovert, and P. M. Adler, Eng. Geol. (Amsterdam) **48**, 283 (1997).
[57] M. K. Davie and B. A. Buffet, Earth Planet. Sci. Lett. **206**, 51 (2003).
[58] P. K. Egeberg and G. R. Dickens, Chem. Geol. **153**, 53 (1999).
[59] G. W. Claypool and I. R. Kaplan, in *Natural Gases in Marine Sediments*, edited by I. R. Kaplan (Plenum, New York, 1974), pp. 19–139.
[60] R. D. Hyndman and E. E. Davies, J. Geophys. Res. **97**, 6683 (1992).
[61] J. H. van der Waals and J. C. Platteeuw, Adv. Chem. Phys. **2**, 1 (1959).
[62] M. B. Clennell, M. Hovland, J. S. Booth, P. Henry, and W. J. Winters, J. Geophys. Res. **104**, 22985 (1999).
[63] I. N. Tsimpanogiannis, Y. C. Yortsos, and P. C. Lichtner, Abstracts of Papers of the 229th ACS National Meeting, San Diego, CA, 2005, 229, U593.
[64] A. G. Yiotis, A. G. Boudouvis, A. K. Stubos, I. N. Tsimpanogiannis, and Y. C. Yortsos, Phys. Rev. E **68**, 037303 (2003).
[65] D. Stauffer and A. Aharony, *Introduction to Percolation Theory* (Taylor & Francis, London, 1992).
[66] S. Bakke and P.-E. Oren, SPEJ **2**, 136 (1997).
[67] W. H. Press, S. A. Teukolsky, W. T. Vettering, and B. P. Flannery, *Numerical Recipes*, 2nd ed. (Cambridge University Press, New York, 1994).
[68] J. Hoshen and R. Kopelman, Phys. Rev. B **14**, 3438 (1976).
[69] D. Wilkinson and J. F. Willemsen, J. Phys. A **16**, 3365 (1983).
[70] J. M. Smith and H. C. Van Ness, *Introduction to Chemical Engineering Thermodynamics*, 4th ed. (McGraw-Hill, New York, 1987).
[71] V. Frette, J. Feder, T. Jossang, and P. Meakin, Phys. Rev. Lett. **68**, 3164 (1992).
[72] P. Meakin, J. Feder, V. Frette, and T. Jossang, Phys. Rev. A **46**, 3357 (1992).
[73] R. M. Ruef, E. D. Sloan, and V. F. Yesavage, AIChE J. **34**, 1468 (1988).
[74] I. N. Tsimpanogiannis, Y. C. Yortsos, and P. C. Lichtner (unpublished).
[75] H. C. Kim, P. R. Bishnoi, R. A. Heidman, and S. S. H. Rizvi, Chem. Eng. Sci. **42**, 1645 (1987).
[76] I. N. Tsimpanogiannis, Y. C. Yortsos, and P. C. Lichtner (unpublished).